Fracture Mechanics of Concrete and Concrete Structures -
Recent Advances in Fracture Mechanics of Concrete - B. H. Oh, et al.(eds)
ⓒ 2010 Korea Concrete Institute, Seoul, ISBN 978-89-5708-180-8

Analysis of X-ray tomographic images of concrete after severe triaxial loading

C. Poinard, Y. Malécot & L. Daudeville
University Joseph Fourier, laboratoire 3SR, Grenoble, France

E. Landis
University of Maine, Maine, USA

ABSTRACT: The stress strain behavior of concrete under triaxial loading is strongly dependent on confining pressure. Specifically, we observe a ductile response at very high pressure, as compared to the brittle or quasi-brittle response we observe in unconfined stress states. This study is intended to examine the meso-structural mechanisms for hydrostatic and triaxial tests. To do this we combine two advanced laboratory instruments: a high pressure triaxial press and an x-ray computed tomography instrument. The laboratory protocol consisted of scanning the concrete prior to the first loading (undamaged) and after each cycle. The analysis of the resulting 3D images shows a high hydrostatic loading upper to 400 MPa damages significantly the cement paste at the mesoscopic scale. For two triaxial tests at 50 and 650 MPa of confining pressure, the results show a strong difference in both damage and failure mechanisms. For the lowest pressure, the shear loading creates localized failure mechanism characterized by a sliding plan angled. For the high pressure, the strain and the damage mode are much more homogeneous with a failure that appears in a high porosity zone.

1 INTRODUCTION

When subjected to violent explosion or ballistic impact, concrete undergoes very severe triaxial stress states (Zukas 1992). The understanding of concrete behavior under such loadings requires the analysis of triaxial tests that enable reproducing the complex loading paths described earlier. Previous experimental studies have revealed the transition from brittle to ductile behavior characterizing cohesive materials, the evolution of limit states and the modification of the facies of failure at very high confining pressures (Sfer et al. 2002, Schmidt et al. 2008, Gabet et al. 2008, Poinard et al. 2008).

Recent experimental and numerical studies (Dupray et al. 2009, Malécot et al. 2009, Vu et al. 2009) have shown a major influence of the granular skeleton on the behavior of concrete under very high confinement contrarily to the well-known low confinement situations where the cement past quality has the main influence on strength.

Following to these results, this paper intends to study the meso-structural mechanism of damage under hydrostatic and triaxial loadings. Thus, two advanced laboratory instruments are combined: a high pressure triaxial press capable of 1 GPa confining pressures, and an x-ray Computed Tomography (CT) instrument that can produce 3D images of internal structure at a resolution approaching 50 µm. CT was strongly used for last years in materials science, it appears as a very powerful tool to track strain localization in geomaterials (Bentz et al. 2000, Desrues et al. 2003). For cementitous materials, Landis used CT to quantify the crack development and damage variables at different cracking levels (Landis et al. 2007).

In this study, the laboratory protocol consists of first making a CT scan of an undamaged concrete cylinder, then making subsequent scans after the cylinder was subjected to load-unload cycles. This kind of test allows seeing the structure evolution of concrete at the mesoscopic scale. Among other things, damage phenomena are described and the air bubble porosity is quantified after each cycle. The two tested specimens have shown the strong role of the air bubble porosity on the hydrostatic behavior at high confining pressure. The triaxial tests realized at low and high confinements highlight different damage modes. At low confining pressure, failure is associated to a very localized damage mechanism. At very high confinement, concrete behaves like a non-cohesive granular staking, and failure is associated to a strong compaction.

2 EXPERIMENTAL SET-UP

2.1 *Triaxial Press*

The tests have been conducted with a high-capacity triaxial press that allows loading a 7 cm in diameter and 14 cm long cylindrical concrete specimen. This press is able to generate a confining pressure up to 0.85 GPa and an axial stress up to 2.3 GPa with a specimen diameter of 7 cm. A Linear Variable Differential Transformer (*LVDT*) linear position *sensor* located in the pressure cell is used to control the axial jack displacement, while a load sensor and a pressure sensor also located in the confinement cell display the stress state of the sample. The confining pressure and axial jack displacement are servo-controlled, which offers the possibility of creating different loading paths. Some more details on this device are given in Gabet et al. (2006).

2.2 *Concrete Samples*

The concrete composition, identical to the one used by Gabet et al. (2006) and and Vu et al. (2009), is shown in Table 1. After pouring, the concrete blocks were conserved for one month in water and then machined and dried at 50°C for two months in an oven. With such a drying process that does not damage the material, the saturation level of concrete specimens is approximately equal to 11%.

The strain level is measured by means of the axial LVDT sensor rather than strain gages that lead to artefacts on CT images. It was shown (Gabet et al. 2006, Dupray et al. 2009) that the friction effect at the specimen ends can be neglected during triaxial tests at high confinement.

Table 1. Compositions and mechanical properties of the studied concrete.

Concrete composition	kg/m^3
0.5/8 "D" gravel	1008
1,800 µm "D" sand	838
CEM I 52.5 N PM ES CP2 cement (Vicat)	263
Water	169
Density	2278
Mechanical properties of the concretes	
Average tested strength after 28 days (MPa)	29
Average slump measured using the Abrams cone (cm)	7
Volume of occluded air measured in fresh concrete (%)	3.4
Porosity accessible to water (%)	12
W/C ratio	0.64
Cement paste volume V_p (m^3/m^3)	0.252

2.3 *Tests*

In this study, hydrostatic and triaxial tests with load and unload cycles are carried out. The concrete specimen is scanned prior to the first loading (undamaged) and after each unloading. The triaxial compression test starts by an hydrostatic loading path. Once the desired confinement has been reached, the specimen is then loaded axially at constant confining pressure (Fig. 1).

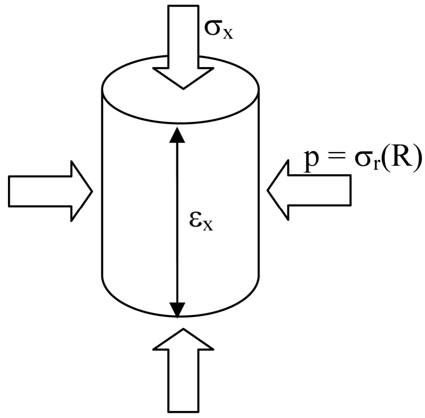

Figure 1. Scheme representing stresses and the measured strain of the sample.

In this paper, compressive stresses and contraction strains are assumed to be positive; σ_x is the principal axial stress, p the pressure inside the confining cell. σ_m the mean stress and q the principal tress difference (deviatoric stress).

$$\sigma_m = \frac{\sigma_x + 2p}{3} \tag{1}$$

2.4 *The CT machine*

This multi-scale X-ray tomograph allows studying in-situ the behavior of geomaterials. This totally innovative device was designed and manufactured by the Rx solution society. It allows scanning objects from 4 mm diameter to 200 mm with resolutions of 5 and 100 µm respectively.

The X-ray CT is a non-destructive imaging technique that allows characterizing the 3D structure of materials. The X-ray CT results provide images with voxel values representing an approximation of the local density of the material. It's then possible to observe the mesoscopic structure of the scanned object. First, the sample scan provides radiographies that represent the X-ray mass attenuation. The Beer-Lambert law (Equation 2) presents the parameters that depend of the X-ray attenuation, so the thickness of the material and the linear coefficient of attenuation.

$$N = N_0.\exp(-\mu.x) \tag{2}$$

N_0 : Number of photon emitted by the source
N : Number of photon passed over the studied object
μ : Linear coefficient of attenuation
x : Thickness of the materiel to pass over

Then, mathematical algorithms allow obtaining the linear coefficient of attenuation μ in each horizontal slice. This parameter being related to the mass density, each voxel is a value close to the average of mass densities of components existing in the voxel.

3 IMAGE ANALYSIS TECHNICS

3.1 *Observation of Damage and Localized Mechanisms*

The goal of this paper is the analysis of damage and localized phenomena evolutions during the cyclic tests. Identical slices are compared before and after each load-unload cycle. The 52 µm of resolution allows apprehending the mechanisms existing at the mesoscopic scale (aggregate size) then associating them to the macroscopic behavior.

This part of the paper shows the modifications applied to the whole images from CT in order to improve the quality of the images studied by eyes. The process contains simply in modifying both contrast and luminance in such way to study only the grey level corresponding on the concrete structure. The Figure 2 exhibits the same horizontal cut before and after processing, the membranes are not existing anymore and the different parts of the concrete are better visible. The images from all the scans will be modified with this process and then compared to identify the modification of the structure.

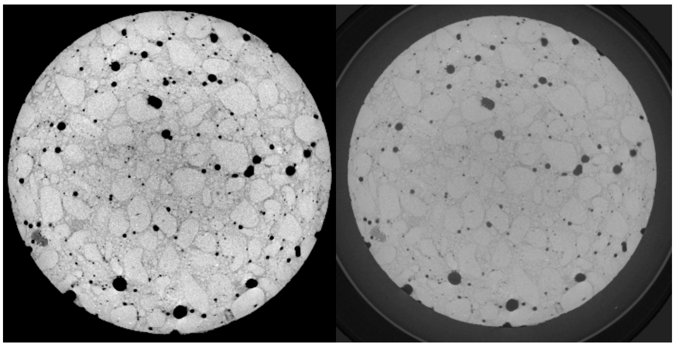

(a) (b)

Figure 2. Slice of concrete specimen with his grey level histogram before (a) and after (b) modification of both contrast and luminance.

3.2 *Porosity Evolution*

The concrete porosity depends on many choices made during the formulation and the way that has been done. However, the different kinds of porosity are identical, just their proportion differ. The less important and the thinnest porosity correspond on the aggregates one, besides it has none role on the vulnerability of the concrete. The both class of pores existing in the cement past are the gel porosity (<3ηm) and the capillary porosity (<10µm). The last class corresponds to the air bubble created while making the concrete. Its rather spherical shape and its mean dimension close to the millimeter make it as the porosity identifiable in the CT images (Fig. 5).

The analysis presented in this part allows to isolate and to quantify the air bubble porosity by applying an image processing to the CT images. By making this analysis on the undamaged specimen and after each load-unload cycle, the evolution of the air bubble porosity is highlighted for both different kind and level of loading path. This image processing has been realized by Eric Landis and his partners (2000, 2007) to study the behavior of mortar.

The result of the image processing depends on a grey level threshold allowing to differentiate the void and the matter. It has been chosen in order to get, for an undamaged concrete specimen, a porosity close to the 4 % corresponding to the air bubble porosity existing in this concrete.

The segmentation steps of the porosity are presented in Figure 3. The first one consists in detecting the cylindrical outline of each slice (Fig. 3a). The second step, called threshold, uses the grey level threshold to separate the voxels in two classes. Those inferior at this grey level take the zero value (black voxel) while the other ones take the 1 value (white) (Fig. 3b). To finish, the two previous images are combined in order to get only the pores (Fig. 3c).

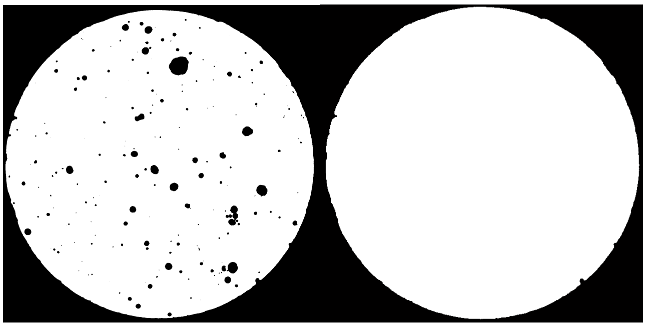

(a) (b)

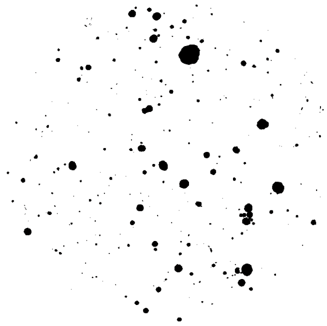

(c)

Figure 3. Steps of porosity segmentation: detection of bounder (a), Threshold (b), image combination (c).

Following to the segmentation, a program allows determining the geometrical features of each pore (volume, exterior surface, spatial coordinates). The method consist in creating a different element for each set of black neighbour voxel, then determining the features of each element by using its own voxels. The segmentation results allow plotting curves such the porosity in the Z direction or even the porosity size distribution. The images representing the cylindrical outline of the sample provide other features like the volume of the concrete.

In this processing, it is necessary to apply a lagrangian description in order to follow the evolution of the initial volume of concrete scanned. To do this, the first and the last slice of each image processing will be the same.

4 TEST RESULTS

4.1 *Hydrostatic Test Up to 650 MPa*

The A8-93 specimen is subjected to three cycles of increasing hydrostatic loading to reach 650 MPa of confining pressure, then a triaxial loading until the failure of the concrete. The Figure 4 exhibits the volumetric behaviour curve for the three first cycles of hydrostatic loading as well as the axial stress - axial strain curve of the entire test. During a hydrostatic loading, the concrete behaves as an isotropic material at the macroscopic scale, so the volumetric strain can be assumed as three times the axial strain.

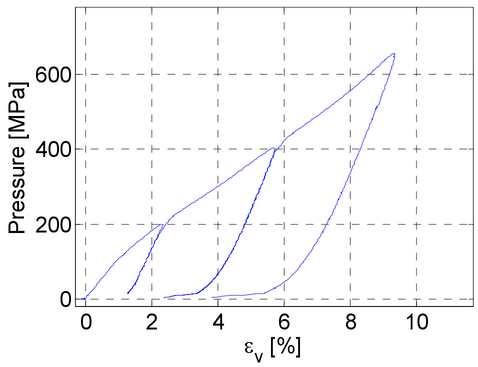

(a)

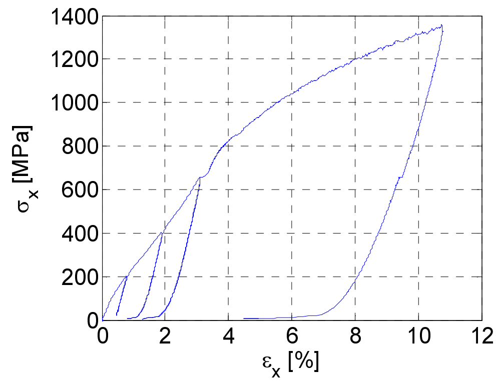

(b)

Figure 4. Volumetric behavior curve of the 3 first hydrostatic loading (a), axial stress σ_x vs. strain components ε_x curve of all the cyclic test (b).

For this experimental campaign, the specimen is taken off the caps to be scanned after each cycle. This handling causes a re-load less steep than the unload because of the new crushing of the concrete-caps interface. In order to get a coherent behaviour, each re-load is fitted on the previous unload. The cycles of hydrostatic loading up to 650 MPa of confining pressure show the main features of hydrostatic tests on concrete. The upper envelope of the volumetric behavior curve indicates a major modification in the tangent bulk modulus of concrete. A decrease is visible from 80 MPa to 250 MPa after which the concrete tightens. The unloading-reloading cycles are steeper than the upper envelope by reason of the absence of irreversible mechanism during these cycles. As explained previously, the reloads are fitted on the unloads until the maximum level of loading reached during the previous cycle. Then the curve follows the curve obtained without the intermediate unload-reload cycles. The elastic bulk modulus, determined by the linear part of the hydrostatic unload, increases slightly with the confining pressure. This modification, important at the beginning and very weak at the end, is similar to the one observed during a cyclic hydrostatic test on the same material (Poinard et al. 2009).

Figure 5 exhibits the same horizontal slice of the concrete specimen before and after each cycle. Table 2 provides the modification of both porosity and concrete volume after each cycle. The inelastic volumetric strains obtained by the image processing are coherent with the LVDT measurements.

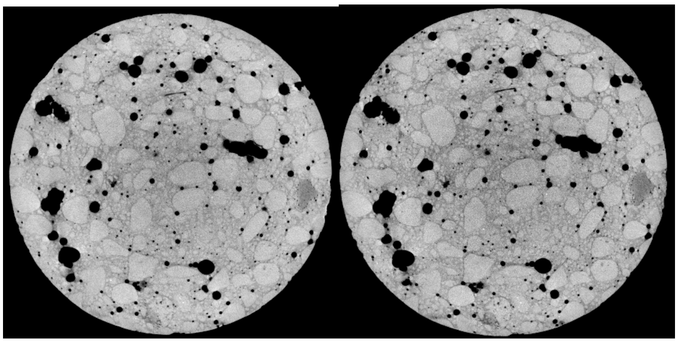

(a) (b)

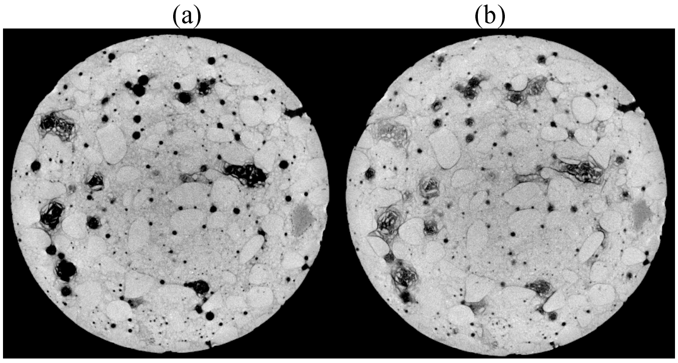

(c) (d)

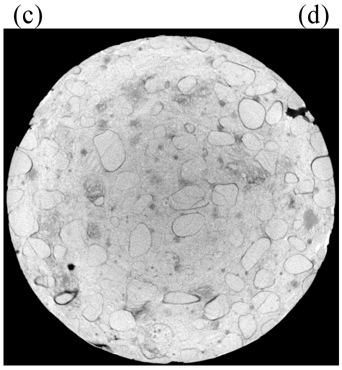

(e)

Figure 5. Same horizontal slice of the A8-93 specimen : undamaged (a), after hydrostatic loading at 200 MPa (b), 400 MPa (c), 650 MPa (d) and after a triaxial loading at 650 MPa of confining pressure until the failure (e).

Table 2. Modification of some features of the A8-93 specimen with the cycles.

Loading path	Undamaged	Hydrostatic			Triaxial
Confinement (MPa)		200	400	650	650
Slice number (± 2)	988	985	980	976	957
Concrete volume* (cm³ ± 0.2)	202	200	196.5	193.5	
Air bubble porosity* (%)	4.2	3.8	2.4	0.5	0.17
Volumetric Strain * (% ± 0.1)	0	1	2.7	4.2	
Volumetric Strain ** (% ± 0.5)	0	1.2	2.5	4	

* Image processing measure
** LVDT measure

After the unloading-reloading cycle at 200 MPa of confining pressure, the images do not show any significant modification of the concrete structure. Although, the closure mechanisms of the porosity are already present (anelastic volumetric strain equal to 1.2 %), the decrease of the air bubbles volume is only 0.4 %. This difference means the collapse of the porosity happens mainly in the cement matrix. The next cycle at 400 MPa of confinement leads to a real damage of the structure (Fig. 5c). The filling up of big pores with debris creates the opening of thin cracks in the matrix. The porosity size distribution of the air bubble is then modified: decrease in the number of big pores and strong increase of the small ones (Fig. 6b). There are also cracks in some of the aggregates and debounding between some of them and the cement matrix. These damage phenomena observed in the entire scanned zone grow with the confining pressure up to 650 MPa. Fig. 6a shows the porosity distribution in the sample in Z direction after each cycle. This Figure shows that the slight non-homogeneity observed in the undamaged sample disappears with the loading increase and the closure of the porosity.

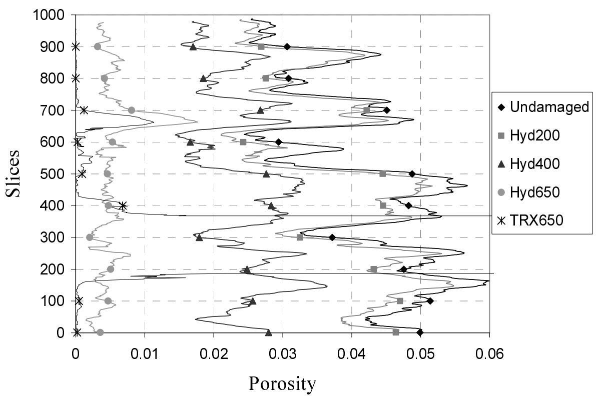

(a)

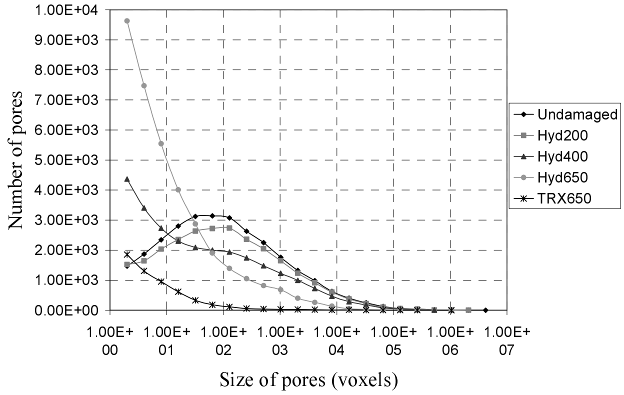

(b)

Figure 6. Change of porosity of the A8-93 specimen with the cycles : porosity in Z direction curve (a), size distribution of pores upper than 1 voxel (b).

4.2 *Triaxial Tests*

4.2.1 *Triaxial Test at 650 MPa of Confining Pressure*

After the hydrostatic loading, the A8-93 specimen is subjected to an additional axial loading under a confining pressure of 650 MPa. This axial loading is increased until the failure of the sample. The axial behaviour is exhibited on the Figure 4b. It is characterised by a very high initial tangent modulus that decreases with the axial loading. One can notice that the rupture of the sample, at the end of the test, is not associated with a plateau of the axial stress.

The axial compression of the specimen while holding the pressure causes a very important compaction of the concrete. There is a big collapse of the porosity (Fig. 6a), the measure of the air bubble porosity is only 0.17 % (Table 2) and the cement matrix appears clearly denser. The damage of the sample is then very significant: a lot of cracks in the aggregates and debounding between the cement matrix and the aggregates are observed (Fig. 5e). During this last load-unload cycle, the growth of a big crack, almost perpendicular to the axial compression direction, cuts the specimen in two parts. The Figure 7 exhibits the same vertical slice of the undamaged sample (a) before (b) and after the axial loading (c). It is worth noticing that the crack avoids aggregates and appears in a high porosity zone (Fig. 6a). The other part of the sample does not exhibit any cracks except small ones very close from the large one.

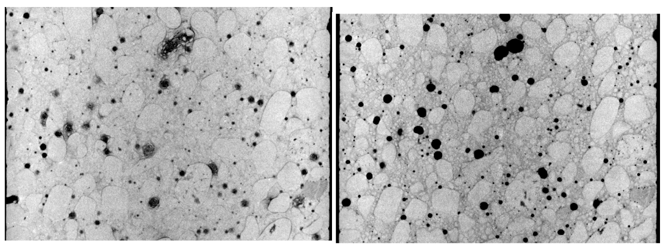

(a) (b)

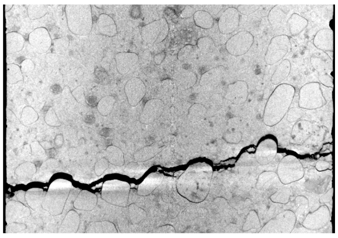

(c)

Figure 7. Same vertical cut of the A8-93 specimen: undamaged specimen (a), after the hydrostatic loading at 650 MPa (b), after the triaxial test at 650 MPa (c).

4.2.2 *Triaxial Test at 50 MPa of Confining Pressure*

The A8-96 specimen is subjected to three successive increases of the axial loadings under a confining pressure of 50 MPa. The Figure 8 exhibits the axial stress-strain curve of the entire test. The envelope of the axial behaviour is similar to the one obtained from monotonous triaxial tests at the same confining pressure. The tangent modulus decreases with the axial strain and the stress peak is clearly visible before the last unloading (end of the test). This peak happens simultaneously as the transition from contractive to dilative behaviour.

Each unloading-reloading cycle provides the axial elastic stiffness defined by the mean slope of the unloading part of the curve. The damage commonly characterised by the decrease of this axial elastic stiffness is not observable before the peak. After the peak the decrease of the slope is still limited due to the inhibition created by the confinement whereas the hydrostatic part of the unloading highlights this damage through a strong non-linearity.

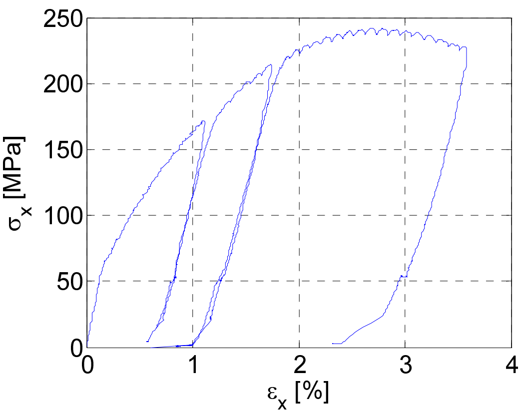

Figure 8. Axial stress - axial strain curve of the A8-96 specimen.

Table 3 and Figure 9 show the evolution of the porosity and of the residual volume of the concrete sample. This specimen was scanned in two parts, so the slice number is two times more important than for the previous specimen. This measurements as well as the tomographic views of the sample show that the damage is very different from the one which was observed with the specimen tested at 650 MPa. Excepted a small decrease of the porosity, any significant modification of the concrete structure appears before the cycle leading to the failure of the specimen.

Table 3. Modification of some features of the A8-96 specimen with the cycles.

Loading path	Undamaged	Triaxial at 50 MPa of confining pressure		
Named	Undamaged	Trx50_1	Trx50_2	Trx50_3
Slice number (± 2)	2322	2318	2308	2268
Concrete volume* (cm³ ± 0.2)	474.9	474.3	472.9	472.4
Air bubble porosity* (%)	3	2.9	2.76	2.1
Volumetric Strain * (% ± 0.04)	0	0.12	0.42	0.52

* Image processing measure

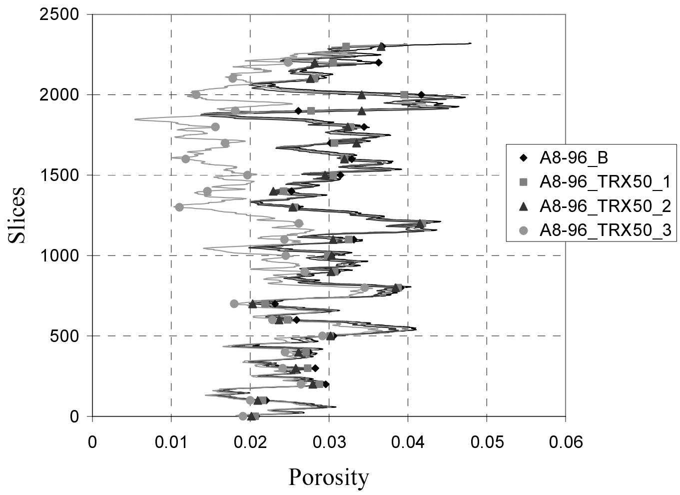

(a)

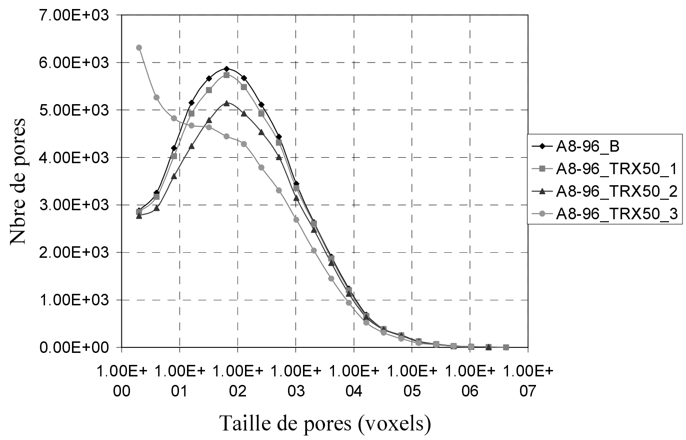

(b)

Figure 9. Change of porosity of the A8-96 specimen with the cycles: porosity in Z direction curve (a), size distribution of pores upper than 1 voxel (b).

During the last cycle, the deviatoric loading creates a very localized damage mechanism. In the highest part of the specimen, the structure is still undamaged. The air bubble porosity remains almost constant (Fig. 9, 10a). On the contrary, in the lower part of the sample, a localized damage is clearly visible. Figure 11 exhibits both the undamaged sample and the sample after failure. A main crack angled at 60 ° crosses over the specimen in the vertical cut (Fig. 11b).

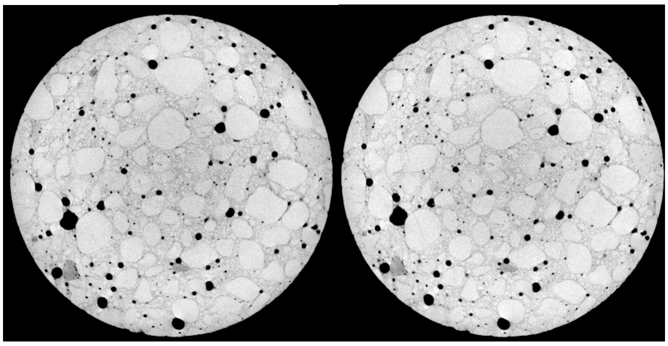

(a) (b)

Figure 10. Same horizontal slice in the high part of the A8-96 specimen: Undamaged (a), after the last cycle (b).

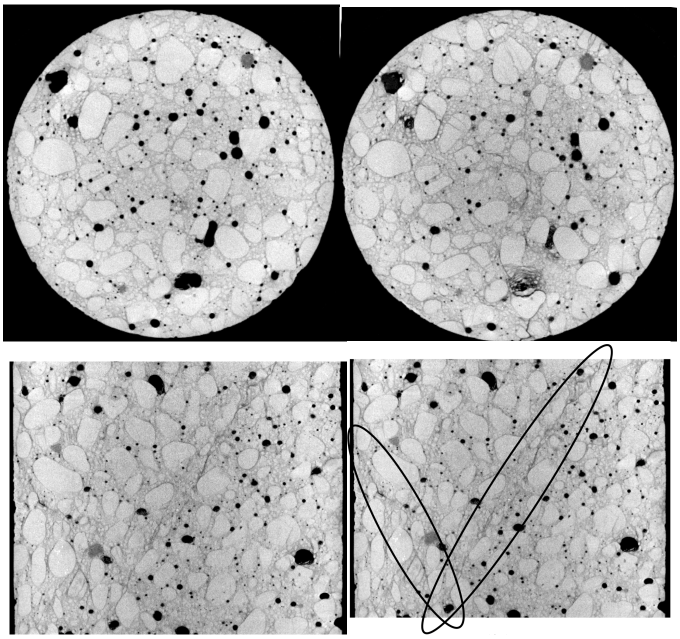

(a) (b)

Figure 11. Same horizontal and vertical slices in the low part of the A8-96 specimen : undamaged (a) and after the last cycle (b).

The analysis of the 3D sample shows others cracks exists close to the main one. The angle of these cracks is also about 60°.

These cracks are very thin but significant enough to create a localized collapse of the air bubble porosity (Fig. 9a). Out of the cracking zone, the structure of the concrete shows a small decrease in porosity. The global porosity distribution is then strongly modified compared to the previous cycles (Fig. 9b). The table 3 highlights an interesting comparison between the drop in air bubble porosity and the increase in volumetric strain. After the first cycle both values match. After the second one, the volumetric strain increases faster than the drop of the porosity. This would suggest that the irreversible volumetric strain is mainly due to the closure of the microporosity of the cement paste. Finally, the failure cycle leads to an important drop in air bubble porosity while the volumetric strain remains almost stable. This last phenomenon is explained by the initiation of thin cracks leading both to a closure of the macroscopic porosity and to a dilative behaviour.

5 CONCLUSION

This paper has focused on highlighting the damage mechanisms of concrete under extreme hydrostatic and triaxial loading. An experimental campaign was carried out on concrete samples thanks to the use of a high capacity triaxial press and an X-ray CT instrument. The tests have consisted of making CT scans of undamaged specimens and making subsequent scans after increasing loading-unloading cycles.

As expected the triaxial damage of concrete is strongly dependent on the confining pressure reached during the hydrostatic phase. For confining pressure higher than 400 MPa, the marks of damage show that under very high hydrostotatic loading the stress states is very inhomogeneous at the mesoscopic scale. It was not expected for this phenomenon to be mainly due to the macroporosity heterogeneity rather than to the one of the aggregates.

For triaxial tests at low confining pressure (around 50 MPa) the cement paste is still very cohesive after the hydrostatic phase. Then, the application of the shear loading creates a localized damage mechanism at the mesoscopic scale. The growth of this mechanism causes a brittle failure of the specimen with a sliding plan angled at 60 °. Out of the failure zone, the concrete remains undamaged at the mesoscopic scale.

For triaxial tests at high confining pressure, the cement paste loses most of its cohesion during the hydrostatic phase. So, the concrete behaves as a noncohesive granular stacking during the axial compression. This feature allows a strong compaction of the concrete specimen before reaching the limit state. Lots of marks of damage appear in both cement paste and aggregates on the entire specimen. An axial compression with such a confining pressure creates a strong granular rearrangement. This rearrangement leads during the unloading to a crack which is almost perpendicular to the axial direction and which is located where the compaction is the strongest.

ACKNOWLEDGMENTS

The GIGA press has been installed in the 3S-R Laboratory within the scope of a cooperative agreement signed with the French Defense Ministry's Armament Division. This research has been performed with the financial support of the Gramat Research Center (CEG, DGA). We would like to thank Dr. Eric Buzaud (CEG) and Dr. Christophe Pontiroli for giving technical and scientific advice.

REFERENCES

Bentz, D.P. Quenard, D.A. Kunze, H.M.P. Baruchel, J. Peyrin, F. Martys, N.S. and Garboczi, E.J. 2000. Microstructure and transport properties of porous building materials. II: Three-dimensional X-ray tomographic studies. *Materials and Structures.* 33 :147

Desrues, J. 2003. X-Ray ct for geomaterials soils, concrete, rocks, International Workshop on X-Ray CT for Geomaterials Kumamoto. November 2003, Japan.

Dupray, F., Malecot, Y., Daudeville, L., Buzaud, E. 2009. A mesoscopic model for the behavior of concrete under high confinement. *International Journal for Numerical and Analytical Methods in Geomechanics*. 33:1407-1423. DOI: 10.1002/nag.771

Gabet T., Vu X.H., Malecot Y. and Daudeville L., A new experimental technique for the analysis of concrete under high triaxial loading, Journal de Physique IV, 2006, 134, 635-644.

Gabet T., Malecot Y., Daudeville L., Triaxial behavior of concrete under high stresses: Influence of the loading path on compaction and limit states, Cement and Concrete Research, 2008, 38(3), 403-412.

Landis, E.N. & Petrell, A.L. & Lu S, & Nagy, E.N. 2000. Examination of pore structure using three dimensional image analysis of microtomographic data. *Concrete Sci Engng.* 2 :162–9.

Landis, E.N. & Zhang, T. & Nagy, E.N. & Nagy, G. & Franklin, W.R. 2007. Cracking, damage and fracture in four dimensions. *Materials and Structures.* 40 :357–364

Malecot, Y., Vu, X.H., Daudeville, L. 2009. Unconfined compressive strength is a poor indicator of the high-pressure mechanical response of concrete. DYMAT 2009, vol. 2 : 1325-1331. DOI: 10.1051/dymat/2009187

Poinard C., Malecot Y., Daudeville L., Damage of concrete in a very high stress state: Experimental investigation, Materials and Structures, 2009, DOI 10.1617/s11527-008-9467-6

Schmidt, M.J. & Cazacu, O. & Green, M.L. 2008. Experimental and theoretical investigation of the high-pressure. *international journal for numerical and analytical methods in geomechanics*

Sfer, D. & Carol, I. & Gettu, R. & Ese, G. 2002. Study of behavior of concrete under triaxial compression. *Journal of Engineering Mechanics* 128(2): 156-163.

Vu X.H., Malecot Y., Daudeville L., Buzaud E., Experimental analysis of concrete behavior under high confinement: Effect of the saturation ratio, International Journal of Solids and Structures, 2009, 46, 1105-1120.

Vu X.H., Malecot Y., Daudeville L., Buzaud E., Effect of the water/cement ratio on concrete behavior under extreme loading, International Journal for Numerical and Analytical Methods in Geomechanics, 2009, DOI: 10.1002/nag.796.

Vu X.H., Malecot Y., Daudeville L., Strain measurements on porous concrete samples for triaxial compression and extension tests under very high confinement *The Journal of Strain Analysis for Engineering Design*, 2009, DOI: 10.1243/03093247JSA547

Zukas, J. A. 1992. Penetration and perforation of solids. Impact Dynamics. Krieger Publishing Company